Available online at www.sciencedirect.com
SCIENCE DIRECT®
Journal of Power Sources 143 (2005) 57–66
JOURNAL OF POWER SOURCES
www.elsevier.com/locate/jpowsour

Improved fuel utilization in microfluidic fuel cells: A computational study

Aimy Bazylak, David Sinton, Ned Djilali*

Institute for Integrated Energy Systems and Department of Mechanical Engineering, University of Victoria, PO Box 3055, STN CSC, Vic., BC, Canada V8W 3P6

Accepted 11 November 2004

Abstract

Presented in this paper is a computational analysis of a membraneless microfluidic fuel cell that uses the laminar nature of microflows to maintain the separation of fuel and oxidant streams. The fuel cell consists of a T-shaped microfluidic channel with liquid fuel and oxidant entering at separate inlets and flowing in parallel without turbulent or convective mixing. Recent experimental studies have established proof-of-concept of such fuel cells and have also shown that their performance is greatly limited by poor fuel utilization. Improving fuel utilization while minimizing fuel-oxidant mixing in microfluidic fuel cells is the focus of this study. A concise electrochemical model of the key reactions and appropriate boundary conditions are presented in conjunction with the development of a computational fluid dynamic (CFD) model of this system that accounts for coupled flow, species transport and reaction kinetics. 3D numerical simulations show that the fuel cell is diffusion limited, and both microchannel and electrode geometry play key roles in system performance. Three cross-sectional geometries are investigated, and a high aspect ratio rectangular geometry results in a two-fold increase in fuel utilization compared to a square geometry with the same hydraulic diameter. By tailoring the flow rate to the axial length of the fuel cell, fuel utilization is increased to 23%. Using the numerical simulation to guide the electrode design process, an extended tapered-electrode design is proposed. Simulations of the tapered-electrode microfluidic fuel cell demonstrate a fuel utilization of over 50%.

Keywords: Membraneless fuel cell; Microfluidic fuel cell; CFD; Laminar flow; Modelling; Simulation

1. Introduction

Micro-sized power sources are needed for small, portable devices capable of operating for long periods without recharging, such as cell phones and laptop computers through to more specialized devices such as remote sensors, global positioning devices, and in vivo diagnostic medical devices. It is predicted [1] that battery technology will not keep pace with these growing portable-power demands, particularly with the next wave of wireless technology, broadband mobile computing. Microstructured fuel cells have the potential to bridge the gap between battery technology and growing portable-power demands, by providing longer duration per weight and volume, quasi-instant recharge, and constant discharge. Recent developments in the field have benefited from micromanufacturing technology and biological and chemical lab-on-a-chip concepts that have been a driving force behind the recent developments of many microfluidic devices [2]. Other emerging application areas for microfluidics include electronic cooling, aerospace, and printing [3].

Since all reactions taking place in fuel cells are surface based, the increase in the surface-to-volume ratio accompanying miniaturization leads to a fundamental improvement in power density [4,5]. There are, however, mechanical limits to the miniaturization of conventional fuel cells [6]: machining graphite bipolar plates becomes difficult, and decreasing the size of the membrane and substrate decreases their support-

* Corresponding author. Tel.: +1 250 721 6034; fax: +1 250 721 6323.
E-mail address: ndjilali@uvic.ca (N. Djilali).

0378-7753/$ – see front matter © 2004 Elsevier B.V. All rights reserved.
doi:10.1016/j.jpowsour.2004.11.029

Nomenclature

A	pre-exponential factor
C_i	concentration of cell i
C_i^{mixed}	concentration of perfectly mixed solution at cell i
C_i^0	concentration of solution at cell i in the absence of mixing
D_i	diffusion coefficient
E	potential at electrode
E_a	activation energy
E_{rev}	reversible potential
F	Faraday constant
h	channel height
J_i	flux of species i
k	rate constant
n	number of electrons
N	total number of cells
P	static pressure
R	gas constant
R_{cell}	ionic resistance of electrolyte
R_i	net rate of production of species i
t	time
T	temperature
U	average fluid velocity
v	rate law
$\vec{v}$	velocity vector
Δx	diffusive mixing region width
y	distance fluid travels downstream
Y_i	local mass fraction of species i

Greek

α	charge transfer coefficient
η	overpotential
ρ	fluid density
υ	kinematic viscosity
χ	apparent reaction order

Chemical formulas

CO_2	carbon dioxide
$(COOH)_{ads}$	adsorbed COOH
e^-	electron
H^+	proton
HCOOH	formic acid
O_2	oxygen
Pt	platinum
Pt^o	occupied platinum site

ing strength. In addition, the performance of miniaturized conventional fuel cells is limited by the Ohmic polarization introduced by the membrane and related water management issues. Novel architectures are crucial for the success of microscale fuel cells [4].

Recently introduced membraneless microfluidic fuel cells [7–9] take advantage of the laminar nature of microflows to maintain the separation of fuel and oxidizer streams without the use of a membrane. A schematic of a microfluidic fuel cell and its operation are given in Fig. 1. The geometry is that of a T-intersection, or T-mixer, which is commonly used in analytical microfluidic chips. The cross-stream mixing rate in such T-intersections is diffusion limited, and many studies have focused on increasing the mixing rate in such geometries [2]. The microfluidic fuel cell, on the other hand, exploits the nature of this flow to achieve the separation of fuel and oxidant streams. The separation of fuel and oxidant is required to restrict reactions of oxidation and reduction to the appropriate electrode. Fuel is introduced at one inlet, and oxidant is introduced at the second inlet. Electrodes are placed along the walls to complete the fuel cell, and oxidation at the anode and reduction at the cathode, together provide the cell potential. The fluid facilitates protonic conduction from one electrode to the other, and the electrons generated at the anode take an external path through an applied load. The length of the reaction channel is limited by the mixing of the two streams. The operation of the fuel cell will begin to fail when the two streams become mixed to the point that oxidation and reduction are no longer restricted to the appropriate electrodes.

Choban et al. [9] were the first to demonstrate a membraneless fuel cell using formic acid and oxygen as reactants. They demonstrated that when two streams are flowing in parallel in the laminar regime, the streams remain separated, eliminating the need for a membrane. Ferrigno et al. [8] demonstrated a millimeter-scale fuel cell using vanadium as reactants. The advantage of this design is that it used the same species (vanadium) as fuel and oxidant, which can be regenerated from a mixture of the products [8]. Choban et al. [7] reported a Y-shaped microfluidic membraneless fuel cell system using formic acid and oxygen as reactants, which reached a current density of 0.4 mA cm^{-2}. The advantage of this system is that it uses acidic solutions to minimize the protonic resistance in the fluid. Both systems [7,8] were reported to be diffusion limited. In this work, a microchannel geometry with a high aspect ratio in the cross-stream direction, similar to that of Ferrigno et al. [8], is investigated, as well as a square geometry similar to that of Choban et al. [7]. Microfluidic fuel cells have several advantages over conventional fuel cells: eliminating the membrane removes related Ohmic losses, water management and sealing issues; and since the fuel and oxidant streams flow together in the same channel network, the fuel cell size is reduced, the design is simplified, and the manifolding requirements are also reduced. In addition, research in this area can capitalize on recent advances in numerical, experimental, and microfabrication techniques [10]. Microfluidic fuel cells have the further advantage of using liquid fuels, which have high energy densities compared to gaseous fuels [1], particularly important in the context of portable-power applications. However, current designs show relatively poor fuel utilization, on the order of 1% [7] to 10% [8]. Microchannel geometries and

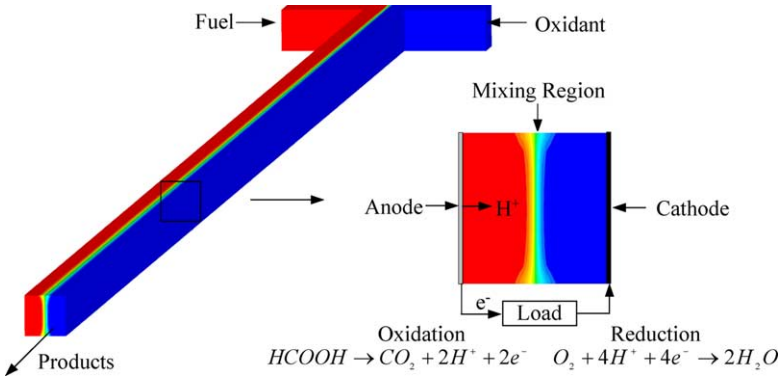

Fig. 1. Numerical simulation and schematic of a microfluidic fuel cell with fuel and oxidant entering at separate inlets and remaining separated as they flow downstream. The flow rates and length scales were selected to illustrate the mixing process.

tailored electrode placements are investigated to considerably improve current designs. Modelling can provide insight into the parameters and geometry required to improve the performance of this technology.

In this work a numerical analysis of a membraneless microfluidic fuel cell is presented. This work is one of the first computational fluid dynamic (CFD) analyses of this technology. The model accounts fully for three-dimensional convective transport in conjunction with anodic and cathodic reaction kinetics. Appropriate boundary conditions for the CFD modelling of this system are developed here and implemented into the numerical model. A numerical investigation of the coupled flow, species transport and electrochemical aspects in this system is conducted. The results provide insight into the running parameters and both microchannel and electrode geometries required to achieve significantly improved performance. Finally, using the numerical simulation to guide the electrode design process, an extended tapered-electrode design is proposed, and its performance is investigated.

2. Hydrodynamic and mass transport model

A three-dimensional CFD model is applied to simulate the coupled flow, species transport, and chemical aspects of the microfluidic fuel cell. Due to the moderate liquid velocities, the internal heating due to viscous dissipation is ignored, and an isothermal system is assumed [3]. The following equations are solved for laminar flow in an inertial reference frame at steady state for incompressible and isothermal fluid flow. Neglecting body forces, the Navier Stokes and continuity equations for incompressible and isothermal flow are given by [11]:

$$\frac{\partial \vec{v}}{\partial t} + \nabla \cdot (\vec{v}\vec{v}) = -\frac{1}{\rho}\nabla P + \nabla \cdot (\upsilon \nabla \vec{v}) \quad (1)$$

$$\nabla \cdot \vec{v} = 0 \quad (2)$$

where P is the static pressure, ρ the fluid density, $\vec{v}$ the velocity vector, and υ the kinematic viscosity. The conservation of species equation is given by

$$\nabla \cdot (\rho \vec{v} Y_i) = -\nabla \cdot \vec{J}_i + R_i \quad (3)$$

where Y_i is the local mass fraction of species i and R_i is the net rate of production of species i by chemical reaction. For the dilute approximation that is used in this model, the diffusion flux of species i is given by Fick's law:

$$\vec{J}_i = -\rho D_i \nabla Y_i \quad (4)$$

where D_i is the diffusion coefficient for species i into the mixture.

3. Reaction model

3.1. Formic acid oxidation

Formic acid is an attractive fuel for fuel cells, as it has been reported to be electrochemically more active than methanol [12]. The oxidation of formic acid is a well-studied, yet complex chemical reaction. The challenge is to provide a reasonable model for this highly non-linear, dual-pathway mechanism [13,14]. A platinum (Pt) catalyst is modelled due to its well-studied nature in regards to formic acid oxidation as well as use in conventional fuel cells.

The oxidation of formic acid (HCOOH) on Pt occurs via a dual pathway mechanism [15]. With the proper catalyst, the oxidation of formic acid favors the direct pathway, the dehydrogenation reaction [15–18] through which carbon dioxide (CO_2) is formed directly according to the generally accepted mechanism proposed by Capon and Parsons [19]:

$$Pt^o + HCOOH \rightarrow (COOH)_{ads} + H^+ + e^- \quad (5)$$

$$(COOH)_{ads} \rightarrow CO_2 + H^+ + e^- + Pt^o \quad (6)$$

The rate determining step occurs between HCOOH and the Pt electrode with the transfer of one electron, as shown in Eq. (5) [14,16]. Modelling the oxidation of formic acid entails the

formulation of the rate constant and rate law governing the reaction. The rate constant in a chemical reaction is given by the Arrhenius equation:

$$k = A\mathrm{e}^{-E_a/RT} \tag{7}$$

where A is the pre-exponential factor, E_a the activation energy, R the gas constant, and T the temperature. The chemical reaction is also governed by the rate law, which is unique to each chemical reaction [20]. The rate law can also be affected by the coverage of platinum sites by carbon monoxide and by $(COOH)_{ads}$ from the second step of the direct pathway, Eq. (6). However, since the second step in the dehydrogenation reaction is believed to be faster than the rate determining step [14], it is assumed that the coverage of platinum sites by $(COOH)_{ads}$ is negligible. It is also assumed that the fuel cell will be operated at a potential where poisoning is not an issue, so that coverage by carbon monoxide is negligible. Therefore, the rate law is given by [14]:

$$v = k[\mathrm{HCOOH}]^{\chi} \exp\left(\frac{\alpha n F\eta}{RT}\right) \tag{8}$$

where [HCOOH] is the concentration of HCOOH in the solution, χ the apparent reaction order, α the charge transfer coefficient, n the number of electrons released at that particular step, F the Faraday constant, and η the overpotential.

In the rate determining step, one electron is released, therefore $n = 1$ in Eq. (8). The reversible potential of formic acid oxidation is $E_{rev} = -0.07$ V (standard hydrogen electrode), so for $E = 0.6$ V reported by Fonseca et al. [16], the overpotential is given by $\eta = 0.67$ V. According to the law of mass action [21], the rate determining step is a first-order reaction, making $\chi = 1$. According to Capon and Parsons [19], the charge transfer coefficient for the oxidation of formic acid on platinum is $\alpha = 0.51$. Similarly, Jiang and Kucernak [14] reported the experimentally determined Tafel slope to be 132 mV dec^{-1} at 60 °C, which resulted in a charge transfer coefficient of $\alpha = 0.497$. The charge transfer coefficient assumed for our model, $\alpha = 0.497$, is in keeping with these works [14,19].

For the rate determining step of the formic acid oxidation reaction, Fonseca et al. [16] reported a rate constant of $k \cong 10^{-2}$ cm s^{-1} on a platinum catalyst modified with lead adatoms at an electrode potential of 0.6 V (normal hydrogen electrode) at 18 ± 2 °C. Pletcher and Solis [17] reported a rate constant for the rate determining step of $k = 1.0 \pm 0.5 \times 10^{-2}$ cm s^{-1} at a potential of 0.6 V at room temperature for the oxidation of formic acid on a platinum anode with lead adatoms. Pletcher and Solis [17] and Fonseca et al. [16] both used the same coverage of 50% of lead adatoms on their Pt surfaces, and obtained rate constants within the same order of magnitude. The rate constant assumed for our model, $k = 1 \times 10^{-2}$ cm s^{-1}, is in keeping with these works [16,17].

3.2. Oxygen reduction

The protons released from the oxidation reaction at the anode diffuse through the solution in the cross-stream direction towards the cathode. At the cathode, the oxygen (O_2) from the oxidant stream, the protons and the electrons that travel through the external circuit combine to produce water in the oxygen reduction reaction:

$$O_2 + 4H^+ + 4e^- \rightarrow 2H_2O \tag{9}$$

Neglecting the structural sensitivity of the Pt surface, a rate constant of $k = 250$ cm s^{-1} is assumed for our model [22]. Based on this assumption, poisoning of the platinum surface is neglected, and the rate law can be written as

$$v = k\,[O_2] \exp\left(-\frac{\alpha F\eta}{RT}\right) \tag{10}$$

where $[O_2]$ is the concentration of O_2 in the solution. The reversible potential for oxygen reduction at standard state is 1.46 V. From the definition of overpotential, $\eta = -0.66$ V at an electrode potential of 0.8 V. At this electrode potential, the charge transfer coefficient is $\alpha = 0.5$ [22].

Both the formic acid oxidation and oxygen reduction reactions were assumed to be first-order reactions. Several assumptions have been made in order to present a reasonable model for the implementation of redox reactions into the computational model. Surface poisoning has been neglected, the dominance of rate determining steps has been assumed, and electrochemical parameters have been approximated based on empirical results.

4. Membraneless microfluidic fuel cell

The model was implemented in Fluent, a commercial finite-volume based CFD package. Dual processors were used to calculate the solutions generated from a hexagonal mesh, with typical run times of 2 h. In all simulations, a hydraulic diameter of 100 μm was used for the inlet and outlet channels. Simulations involving the hydrodynamic and mass transport model are presented, followed by simulations including the reaction model.

The fuel and oxidant cross-stream diffusive mixing was quantified with the hydrodynamic and mass transport model. The operation of the fuel cell will begin to fail when the two streams become mixed to the point that oxidation and reduction are no longer restricted to the appropriate electrodes. The extent to which the fuel and oxidant become diffusively mixed is proportional to the diffusivity of the fuel in the solvent. The diffusivity also affects the mass transport of the fuel to the electrodes. The binary mixture is assumed dilute, and the diffusion coefficient is constant throughout. A diffusion coefficient of $D = 5 \times 10^{-10}$ m^2 s^{-1} is assumed, which is a typical value for the diffusion of relatively small molecules in an aqueous solution [2,20].

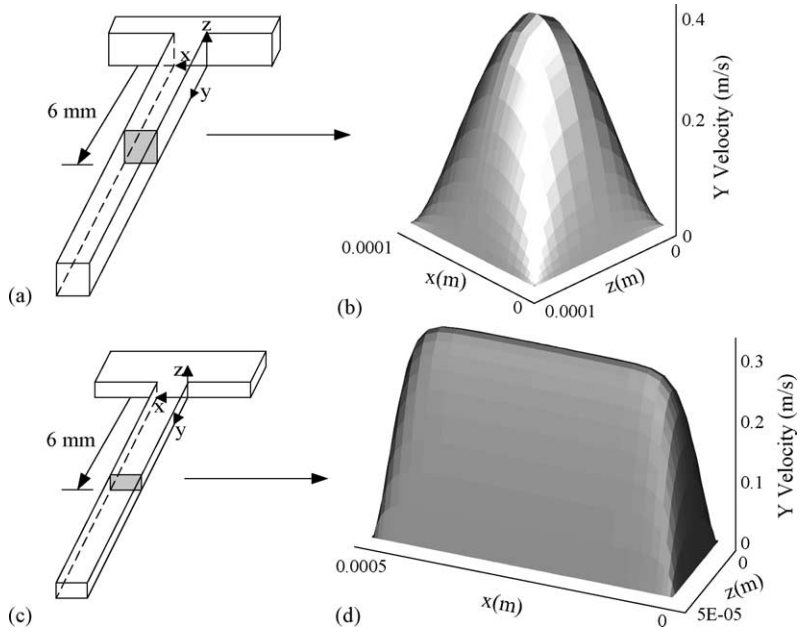

Fig. 2. Liquid transport in the microfluidic fuel cell: (a) schematic illustrating the location of the *X–Z* cross section of interest for the axial velocity contour plot of the square geometry (100 μm × 100 μm), (b) corresponding axial velocity contour plot, (c) schematic illustrating the location of the *X–Z* cross section of interest for the axial velocity contour plot of rectangular geometry (550 μm × 55 μm), and (d) corresponding axial velocity contour plot.

Pressure was applied to drive the flow, and a no-slip velocity condition is applied to the walls. These boundary conditions result in the formation of boundary layers with steep cross-stream velocity gradients, apparent in the velocity profiles plotted in Fig. 2. These cross-stream velocity gradients greatly affect the diffusive mixing. Near the walls, the fluid flows relatively slowly. As a result, cross-stream mixing is more pronounced in the near-wall regions, and the mixing region takes on an hour-glass shape as shown in Fig. 1. The calculated width of the diffusive mixing region at the walls of the fuel cell is in agreement with the theoretically predicted [23] and experimentally validated [8] trend represented by the following expression:

$$\Delta x \approx \left(\frac{Dhy}{U}\right)^{1/3} \tag{11}$$

where h is the channel height, y the distance the fluid flows downstream, and U the average flow speed. Down the center of the channel, the diffusive mixing region grows more slowly, following a one-half power scaling [23]. Several works have focused on the inclusion of electrokinetic phenomena in microfluidic systems [24–26], but due to the high ionic concentrations employed here, electrokinetic effects

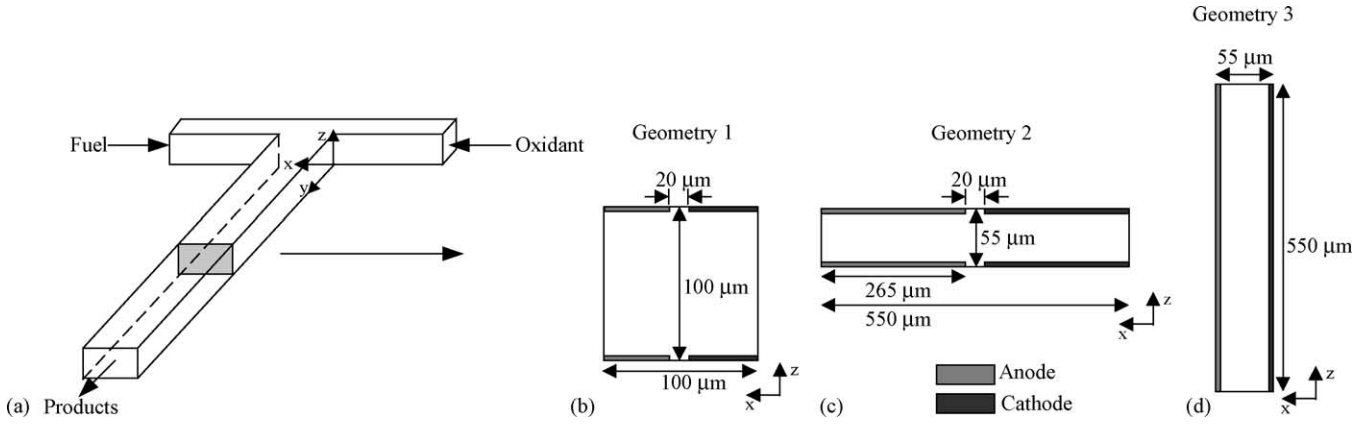

Fig. 3. A schematic diagram of the microfluidic fuel cell system: (a) the location of the *X–Z* cross section of interest, (b) Geometry 1 is square with electrodes placed on the top and bottom channel surfaces, (c) Geometry 2 is rectangular with electrodes placed on the top and bottom channel surfaces, and (d) Geometry 3 is rectangular with electrodes placed along the left and right walls of the channel.

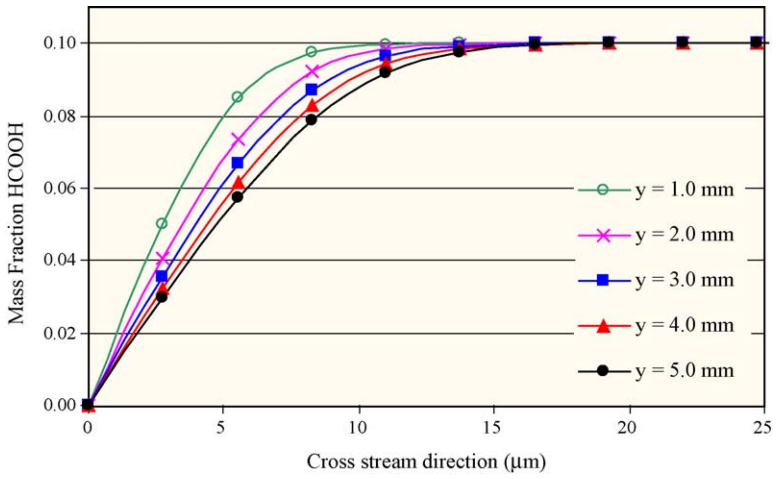

Fig. 4. Formic acid bulk concentration normal to the anode wall for various downstream positions (at the anode midpoint). The concentration is reduced to zero at the electrode surface, indicating that the reaction kinetics are fast compared to the diffusion in this system.

are negligible. The challenges in modelling microfluidic fuel cells lie in capturing the three-dimensional mixing dynamics and the reaction and electrode kinetics.

Fig. 3 shows a schematic of the microfluidic fuel cell with different geometries, all of which have a hydraulic diameter of 100 μm. Geometry 1 shown in Fig. 3(b) and Geometry 2 shown in Fig. 3(c) have electrodes placed along the top and bottom walls with a 20 μm spacing between the electrodes to account for the diffusive mixing regions. A high aspect ratio is used for Geometry 2, and a low aspect ratio is used for Geometry 3, whose electrodes are placed along the left and right walls of the channel.

Fig. 4 shows the concentration profiles of formic acid at the midpoint of the anode when the electrode kinetics were included in the model. The concentration was reduced to zero at the electrode surface, indicating that the reaction kinetics were fast compared to the diffusion in this system. This result is in keeping with experimental results [7,8]. Since the fuel cell is diffusion limited, the geometry of the microchannel plays a predominant role in the efficiency of the cell.

Although the fuel and oxidant streams do not experience turbulent or convective mixing, they do experience diffusive mixing. The formic acid and oxygen concentration boundary layers developed at the electrode surfaces, along with the diffusive mixing regions are illustrated in Figs. 5–7, for Geometries 1–3, respectively. Figs. 5–7(b) shows the formic acid mass fraction contour plot, showing the diffusive mixing between fuel and oxidant streams at the outlet in the absence of electro-oxidation reactions. As expected, the diffusive mixing region takes on an hour-glass shape due to the slower velocities at the walls. Figs. 5–7(c) shows the formic acid mass fraction contour plots combining the effect of diffusive mixing and the electro-oxidation at the anodes. A thicker concentration boundary layer is apparent near the wall adjacent to the electrode surface and is due to the combined wall/end effects. Similarly, Figs. 5–7(d) shows the oxygen mass fraction contour plots combining diffusive mixing and the electro-reduction at the cathode. Due to a constant diffusion coefficient and diffusion limited electrodes, the depletion and mixing of oxygen in (d) is a mirror image of the depletion and mixing of formic acid in (c). In each case the Reynolds number is 20, based on the hydraulic diameter, which is 100 μm in each case. A length of 6 mm downstream was chosen as the outlet in each case for comparison pur-

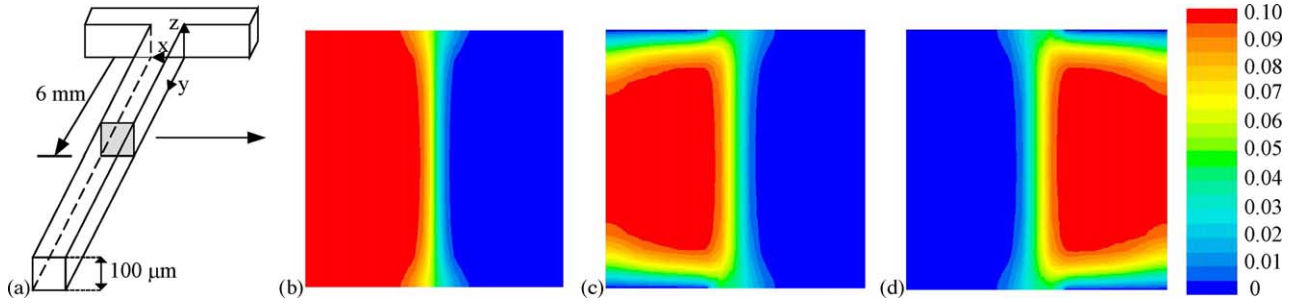

Fig. 5. Depletion and mixing of HCOOH and O_2 in the microfluidic fuel cell with Geometry 1: (a) the location of the *X–Z* cross section of interest, (b) HCOOH mass fraction contour plot showing diffusive mixing between the fuel and oxidant streams without electro-oxidation reactions, (c) HCOOH mass fraction contour plot showing combined diffusive mixing and electro-oxidation at the anodes (top and bottom, left), and (d) O_2 mass fraction contour plot showing combined diffusive mixing and reduction at the cathodes (top and bottom, right).

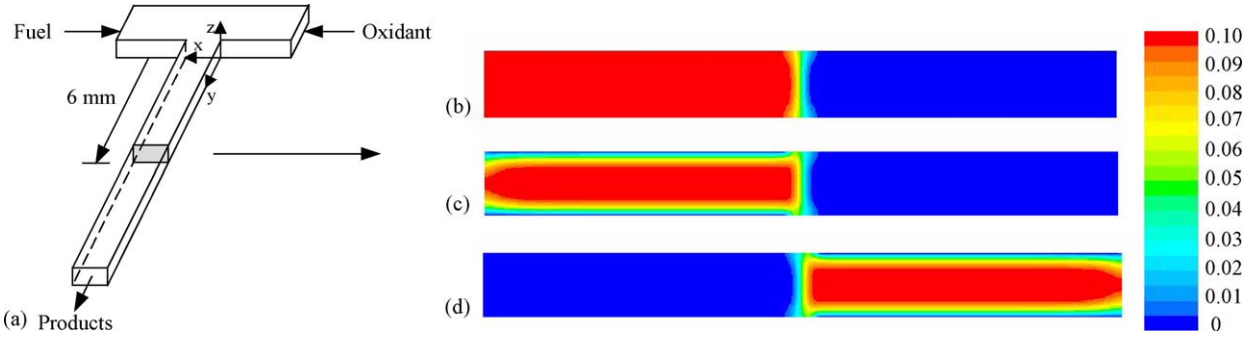

Fig. 6. Depletion and mixing of HCOOH and O_2 in the microfluidic fuel cell with Geometry 2: (a) the location of the *X*–*Z* cross section of interest, (b) HCOOH mass fraction contour plot showing diffusive mixing between the fuel and oxidant streams without electro-oxidation reactions, (c) HCOOH mass fraction contour plot showing combined diffusive mixing and electro-oxidation at the anodes (top and bottom, left), and (d) O_2 mass fraction contour plot showing combined diffusive mixing and reduction at the cathodes (top and bottom, right).

poses. Fuel utilization was determined from the ratio of fuel mass flow rate at the outlet to the fuel mass flow rate at the inlet. With an inlet velocity of 0.1 m s^{-1}, the square geometry provides a fuel utilization of 3%, whereas the rectangular geometries with aspect ratios of 1:10 provide a fuel utilization of 8%. These results are in agreement with recent experimentally determined fuel utilizations on the order of 1% for the square geometry presented by Choban et al. [7] and 10% for the rectangular geometry presented by Ferrigno et al. [8]. Although Geometries 2 and 3 provide similar fuel utilization, there is significantly less cross-stream fuel-oxidant mixing in Geometry 2, illustrated in Fig. 6(b). Both geometries exhibit a mixed region of similar width, but the volume of fluid in the mixed region is significantly less in Geometry 2. The degree to which the reactants are mixed is an indication of how much potential there is for improved fuel utilization. The percentage of mixing is quantified using the following expression [27]:

$$\%\,\text{mixed} = \left(1 - \frac{\sqrt{(1/N)\sum_{i=1}^{N}(C_i - C_i^{\text{mixed}})^2}}{\sqrt{(1/N)\sum_{i=1}^{N}(C_i^0 - C_i^{\text{mixed}})^2}}\right) \times 100 \quad (12)$$

where N is the total number of cells, C_i the concentration of cell i, C_i^{mixed} the concentration of the perfectly mixed solution at cell i, and C_i^0 the concentration at cell i if no mixing or diffusion were to occur. With an inlet velocity of 0.1 m s^{-1}, at the outlet of the fuel cell, Geometries 1–3 resulted in 14%, 8% and 19% mixing respectively (measured at the outlet). These results indicate that particularly for Geometry 2, there is an opportunity to utilize much more fuel.

The effect of the inlet velocity magnitude for Geometry 2 is shown in Fig. 8. With respect to an analysis of fuel utilization and mixing, reducing the inlet velocities is effectively equivalent to increasing the length of the microfluidic fuel cell. Decreasing the inlet velocity from 0.1 to 0.02 m s^{-1} causes the fuel utilization to increase non-linearly from 8% to 23%. This increase in fuel utilization is highly significant in the context of values provided in previous studies [7,8]. The mixing region at the outlet reached 20 μm wide, which is equivalent to the separation distance between the electrodes. Decreasing the inlet velocity further would result in fuel cross-over. It is noteworthy, however, that the percentage mixed at the outlet increased only 3% (from 8% for the 0.1 m s^{-1} inlet velocity to 11% for the 0.02 m s^{-1} inlet velocity), indicating that further improvements in fuel utilization are possible by extending a tapered electrode beyond

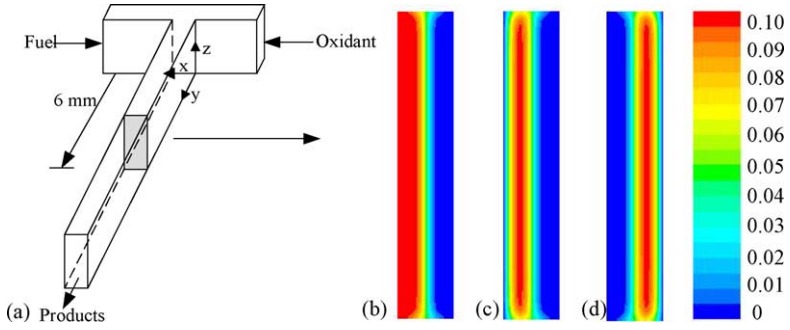

Fig. 7. Depletion and mixing of HCOOH and O_2 in the microfluidic fuel cell with Geometry 3: (a) the location of the *X*–*Z* cross section of interest, (b) HCOOH mass fraction contour plot showing diffusive mixing between the fuel and oxidant streams without electro-oxidation reactions, (c) HCOOH mass fraction contour plot showing combined diffusive mixing and electro-oxidation at the anodes (top and bottom, left), and (d) O_2 mass fraction contour plot showing combined diffusive mixing and reduction at the cathodes (top and bottom, right).

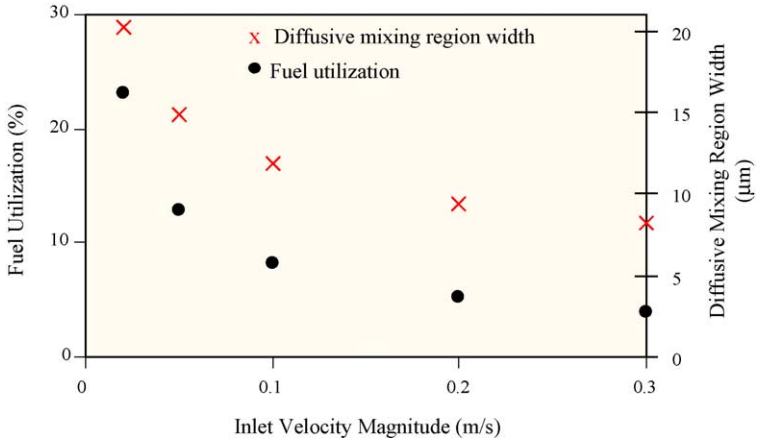

Fig. 8. Effect of increasing the inlet velocity on fuel utilization and diffusive mixing region width for Geometry 2, measured at the outlet of a 6 mm long microfluidic fuel cell.

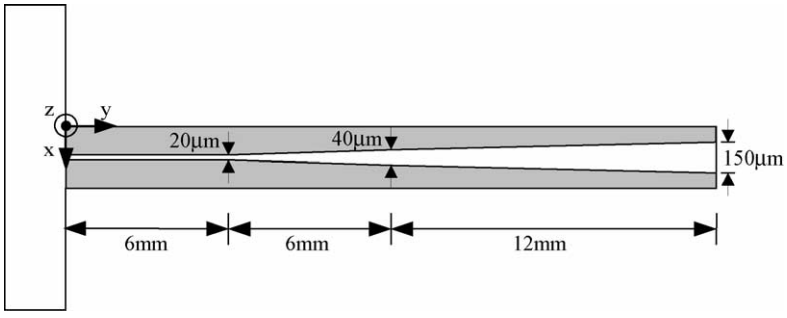

Fig. 9. A Schematic diagram of the microfluidic fuel cell system with Geometry 2 extended with tapered electrodes.

the 6 mm length (while maintaining channel cross-sectional dimensions).

The schematic of Geometry 2 with extended tapered electrodes is given in Fig. 9. The concept is to taper the electrodes to match the growth of the mixing region, and thereby exploit unused and unmixed fuel while avoiding fuel cross-over. With an inlet velocity of 0.02 m s^{-1}, this electrode design results in a fuel utilization increase from 23% to 52%. Fig. 10 illustrates the formic acid and oxygen concentration boundary layers developed at the electrode surfaces, along with the diffusive mixing regions for the extended electrode geometry. Compared to the species mass fraction contour plots shown in Fig. 6, where the fuel cell length extended to only 6 mm, the contour plots shown in Fig. 10 illustrate that the fuel utilization has been significantly improved with the extended geometry and tapered electrodes. Fig. 11 illustrates

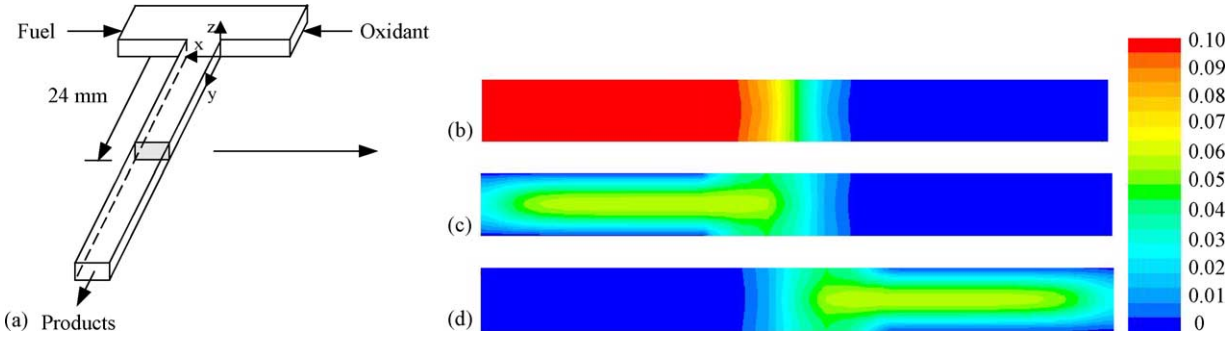

Fig. 10. Depletion and mixing of HCOOH and O_2 in the microfluidic fuel cell with Geometry 2 extended with tapered electrodes: (a) the location of the *X–Z* cross section of interest, (b) HCOOH mass fraction contour plot showing diffusive mixing between the fuel and oxidant streams without electro-oxidation reactions, (c) HCOOH mass fraction contour plot showing combined diffusive mixing and electro-oxidation at the anodes (top and bottom, left), and (d) O_2 mass fraction contour plot showing combined diffusive mixing and reduction at the cathodes (top and bottom, right).

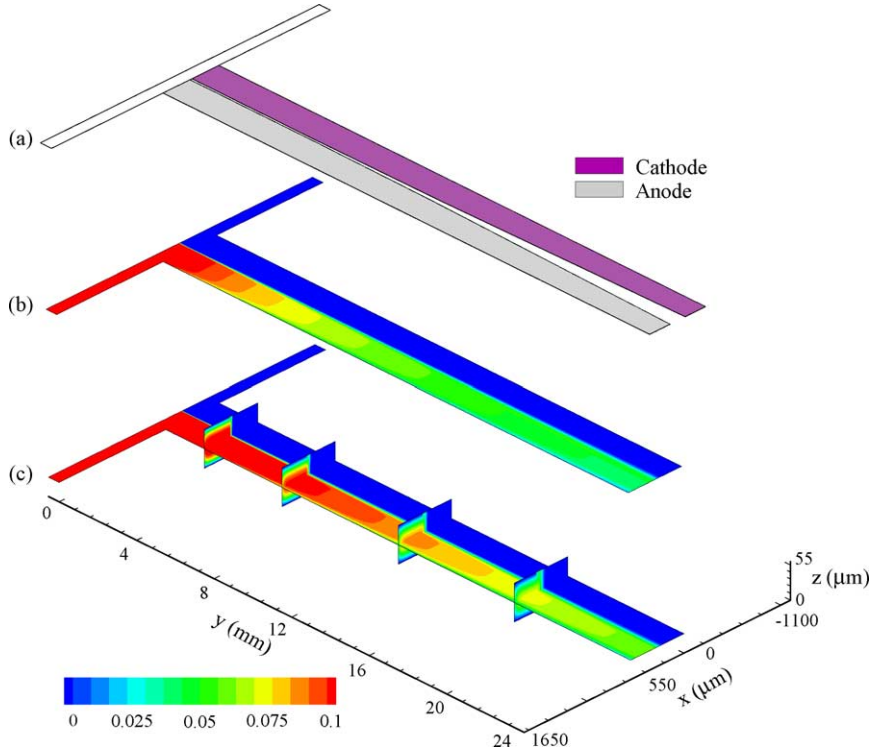

Fig. 11. Depletion of HCOOH in the microfluidic fuel cell with Geometry 2 with tailored electrodes: (a) tailored electrode placement, (b) HCOOH mass fraction contour plot on the *X–Y* plane at $z = 13.75$ μm (quarter plane), (c) HCOOH mass fraction contour plot on the *X–Y* plane at $z = 27.5$ μm (mid-plane) and at *X–Z* planes along the downstream channel ($y = 2$, 6, 12 and 18 mm). Length scales were adjusted to illustrate the depletion of HCOOH in the downstream direction.

the depletion of formic acid as the fuel flows downstream. Fig. 11(a) shows the tailored electrode placement. Fig. 11(b) is the formic acid mass fraction contour plot on the *X–Y* plane at a depth of $z = 13.75$ μm (quarter plane). Fig. 11(c) is the formic acid mass fraction contour plot on the *X–Y* plane at a depth of $z = 27.5$ μm (mid-plane). Due to the concentration boundary layers near the top and bottom walls of the channel, the formic acid concentration is more depleted in the quarter plane compared to the mid-plane. Fig. 11(c) also shows formic acid mass fraction contour plots at *X–Z* planes along the downstream channel at positions $y = 2$, 6, 12, and 18 mm. Similar to the fuel mass fraction contour in the *X–Y* plane, the contours in the *X–Z* planes also illustrate the depletion of formic acid as the fuel travels downstream.

Geometry 2 yields a total current of 0.059 mA, and when this geometry is extended with tapered electrodes the total current increases to 0.13 mA corresponding to an average current density of 1.1 mA cm^{-2}. It is noteworthy that the experimentally measured output power would be expected to be less than the theoretical prediction due to the effects associated with non-constant overpotentials and fluid properties. Furthermore, the resistivity of the fuel cell would change as the liquid flows downstream where the electrolyte concentration weakens. These results indicate that extending the length of the fuel cell geometry with tapered electrodes provides a larger total current and an improved use of reactants.

5. Conclusions

This work is one of the first CFD analyses for this emerging technology. Recent experimental studies have established proof-of-concept results; however, poor fuel utilization greatly limits the performance of current designs. Improving fuel utilization while minimizing fuel-oxidant mixing in the microfluidic fuel cell was the focus of this study. A concise electrochemical model of the key reactions and appropriate boundary conditions for the microfluidic fuel cell have been developed and implemented into the numerical model. A numerical investigation of the coupled flow, species transport and chemical aspects provided insight into the running parameters and cell geometry required to achieve significantly improved performance.

The geometry of the cell plays a critically important role in the performance of the cell, which was limited by the mass transport of reactants through the concentration boundary layers to the electrodes. Three geometries were investigated. The straight and rectangular channel geometries simulated in this study are in keeping with current designs. The rectangular geometry with a high aspect ratio in the cross-stream direction is the most promising design for the microfluidic fuel cell, as the reactants demonstrate the least percentage of mixing and the best fuel utilization at the outlet of the fuel cell. With the same hydraulic diameter as the square geome-

try, the overall fuel utilization increases by more than a factor of two over the square geometry.

Lowering the inlet velocity results in a significant improvement in fuel utilization with a minimal increase in cross-stream mixing at the outlet. Decreasing the inlet velocity from 0.1 to 0.02 m s^{-1} causes the fuel utilization to increase non-linearly from 8% to 23%, and only causes an increase of 3% in cross-stream mixing at the outlet. Power output requirements and the diffusive mixing of fuel and oxidant, however, ultimately limit the degree to which the velocity can be reduced. Based on our analysis, a tapered-electrode design was suggested. Numerical simulations indicate that significant improvements result from the tapering of the electrodes towards the outlet of the microfluidic fuel cell, while maintaining constant channel cross-sectional dimensions. By tailoring the electrode shape to the reactant concentration profile for an extended cell geometry, the fuel utilization increased from 23% to 52%, producing an average current density of 1.1 mA cm^{-2}.

Acknowledgements

The authors are grateful for the financial support of the Natural Sciences and Engineering Research Council (NSERC) of Canada, through a post-graduate scholarship to AB and research grants to DS and ND. Financial support from the University of Victoria, as well as from the Advanced Systems Institute of British Columbia, through post-graduate scholarships to AB are also gratefully acknowledged.

References

[1] C.K. Dyer, J. Power Sources 106 (2002) 31–34.
[2] H.A. Stone, A.D. Stroock, A. Ajdari, Annu. Rev. Fluid Mech. 36 (2004) 381–411.
[3] K.V. Sharp, R.J. Adrian, J.G. Santiago, J.I. Molho, in: M. Gad-el-Hak (Ed.), The MEMS Handbook, CRC Press, Boca Raton, FL, USA, 2002, pp. 6-1, 6-2, 6-4.
[4] G.F. McLean, N. Djilali, M. Whale, T. Niet, Proceedings of the 10th Canadian Hydrogen Conference, 2000, pp. 349–358.
[5] R. Hahn, S. Wagner, A. Schmitz, H. Reichl, J. Power Sources 131 (2004) 73–78.
[6] S.J. Lee, A. Chang-Chien, S.W. Cha, R. O'Hayre, Y.I. Park, Y. Saito, F.B. Prinz, J. Power Sources 112 (2002) 410–418.
[7] E.R. Choban, L.J. Markoski, A. Wieckowski, P.J.A. Kenis, J. Power Sources 128 (2004) 54–60.
[8] R. Ferrigno, A.D. Stroock, T.D. Clark, M. Mayer, G.M. Whitesides, J. Am. Chem. Soc. 124 (2002) 12930–12931.
[9] E.R. Choban, L.J. Markoski, J. Stoltzfus, J.S. Moore, P.A. Kenis, Power Sources Proc. 2002 40 (2002) 317–320.
[10] J.C. McDonald, D.C. Duffy, J.R. Anderson, D.T. Chiu, H.K. Wu, O.J.A. Schueller, G.M. Whitesides, Electrophoresis 21 (1) (2000) 27–40.
[11] R.B. Bird, W.E. Stewart, E.N. Lightfoot, Transport Phenomena, Wiley, New York, 1960, pp. 81, 83.
[12] M. Weber, J.-T. Wang, S. Wasmus, R.F. Savinell, J. Electrochem. Soc. 143 (7) (1996) L158–L160.
[13] S.G. Sun, Y.Y. Yang, J. Electroanal. Chem. 467 (1999) 121–131.
[14] J. Jiang, A. Kucernak, J. Electroanal. Chem. 520 (2002) 64–70.
[15] C. Rice, S. Ha, R.I. Masel, P. Waszczuk, A. Wieckowski, T. Barnard, J. Power Syst. 111 (2002) 83–89.
[16] I. Fonseca, J. Lin-Cai, D. Pletcher, J. Electrochem. Soc. 130 (11) (1983) 2187–2192.
[17] D. Pletcher, V. Solis, J. Electroanal. Chem. 131 (1982) 309–323.
[18] P. Waszczuk, T.M. Barnard, C. Rice, R.I. Masel, A. Wieckowski, Electrochem. Commun. 4 (2002) 599–603.
[19] A. Capon, R. Parsons, Electroanal. Chem. Interfacial Electrochem. 43 (1973) 205–231.
[20] J.H. Espenson, Chemical Kinetics and Reaction Mechanisms, 2nd ed., McGraw-Hill, New York, 1995, 200 p.
[21] H.C. Metcalfe, J.E. Williams, J.F. Castka, Modern Chemistry, Holt, Rinehart and Winston, Inc, New York, 1970, 412 p.
[22] N.M. Markovic, P.N. Ross Jr., in: A. Wieckowski (Ed.), Interfacial Electrochemistry: Theory, Experiment, and Applications, Marcel Dekker, New York, 1999, pp. 821–841.
[23] R.F. Ismagilov, A.D. Stroock, P.J.A. Kenis, G. Whitesides, Appl. Phys. Lett. 76 (17) (2000) 2376–2378.
[24] Z. Adamczyk, P. Warszynzki, M. Zembala, Bull. Pol. Acad. Sci. Chem. 47 (3) (1999) 239–258.
[25] D. Erickson, D. Li, Langmuir 18 (2002) 1883–1892.
[26] D. Erickson, D. Li, J. Phys. Chem. B 107 (2003) 12212–12220.
[27] T.J. Johnson, D. Ross, L.E. Locascio, Anal. Chem. 74 (1) (2002) 45–51.